Ultrastructural Perspectives on the Biology and Taphonomy of Tonian Microfossils From the Draken Formation, Spitsbergen

Alexandre Fadel, Kevin Lepot, Sylvain Bernard, Ahmed Addad, Armelle Riboulleau, Andrew H. Knoll

Microfossil fragmentation across the Paleocene-Eocene transition at ODP Site 1209 (North Pacific): implication for reconstructing nannofossil fluxes.

Nicolas Pige[1*], Guillaume Suan[1], Eddy Buiron[1], Vincent J. Langlois[1], Alyssa Mehir[1], Arnauld Vinçon-Laugier[1], Emanuela Mattioli[1,2]

[1] Univ Lyon, UCBL, ENSL, UJM, CNRS, LGL-TPE, F-69622, Villeurbanne, France

[2] Institut Universitaire de France (IUF)

*corresponding author: nicolas.pige@univ-lyon1.fr

Abstract

The Paleocene-Eocene period was punctuated by several hyperthermal events likely triggered by massive injection of greenhouse gases, the best-known being the PETM (~56 Ma). Environmental changes during hyperthermals severely impacted planktonic organisms, especially calcareous nannoplankton producing tiny calcite platelets. These calcite platelets (coccoliths) accumulate at the sea floor and constitute a major component of deep-sea sediments. As calcareous nannoplankton contribute to the biological carbon pump and carbonate counter pump, a better knowledge of their production dynamics in surface ocean and their dissolution throughout the water column is pivotal to produce realistic carbon budgets across hyperthermal events. In this work, we quantitatively assessed calcareous nannofossil abundances and nannofossil fragments from deep sea sediments of late Thanetian to early Ypresian age (55.63-57.42 Ma) from ODP Site 1209 (North Pacific). We developed a new method, based on the shape and number of fragments, to reconstruct an

all-inclusive nannofossil absolute abundance (including entire specimens and fragments) in the sediments. The reconstructed values of absolute abundance estimated integrating fragments are on average 25% higher. We also analysed different dissolution proxies (planktonic fragmentation, benthic/planktonic ratios, coarse fraction). The fragmentation of planktonic foraminifera does not covary with nannofossil fragmentation, suggesting distinct controlling factors. Foraminiferal proxies and nannofossil assemblages point to episodes of intense dissolution across the PETM as well as during an event pre-dating the PETM by 300-700 kyrs that we identify as the Late Paleocene Event (LPE).

Keywords: Carbon cycle, Paleocene-Eocene transition, Calcareous nannofossils, Dissolution, Fragmentation

1. Introduction

The Paleocene-Eocene Thermal Maximum (PETM; around 56 Ma) is considered as one of the best analogues of the ongoing global warming and ocean acidification (Kennett and Stott, 1991; Zachos et al., 2005; Luo et al., 2016; Westerhold et al., 2018). The PETM is characterised by a global 3 to 4‰ negative $\delta^{13}C$ excursion recorded in deep-sea calcium carbonate ($CaCO_3$). It is associated with a sharp decrease in $CaCO_3$ content in deep-sea sediments, which is interpreted as a result of shoaling of the lysocline and CCD (carbonate compensation depth), following massive CO_2 injections and oceanic acidification (Zachos et al., 2005; Zeebe et al., 2012). The PETM is preceded and followed by several other hyperthermal events of smaller amplitude and shorter duration (Cramer et al., 2003; Barnet et al., 2019).

Rapid environmental changes during the PETM impacted marine organisms, including coccolithophores, unicellular photosynthetic algae using CO_2 for photosynthesis and producing calcite platelets named coccoliths. Coccoliths, having a size range between 2 and 20 µm (Young and Ziveri, 2000), settle from the surface layers of the oceans down to the surface sediment incorporated in faecal pellets or marine snow (e.g., Honjo, 1976), and constitute a major component of pelagic carbonates. Coccolith carbonate represents between 20 to 80% of the biogenic $CaCO_3$ burial, for a total annual $CaCO_3$ mass burial of about $1.3E^{12}$ kg (e.g., Baumann et al., 2004; Hay, 2004; Balch et al., 2007; Ziveri et al., 2007). Hence, coccolith-produced carbonates represent one of the largest carbon sinks on Earth on geological timescales. The burial of $CaCO_3$ is controlled by four distinct but complementary mechanisms (e.g., Roth and Thierstein, 1972; Schlanger and Douglas, 1974; Honjo, 1976; Honjo and Herez, 1976; Archer and Maier-Reimer, 1994; Milliman, 1999; Langer et al., 2007; Cartapanis et al, 2018; Sulpis et al., 2021): I) the $CaCO_3$ production in the surface oceanic layer, depending on environmental (nutrients availability, temperatures, salinity, alkalinity) and biological (ecology of dominant groups) factors; II) the export of these particles to the deep ocean, which is essentially dependent on biological factors (grazing, bacterial activities) and temperature; III) dissolution processes within the water column and at the seafloor, constrained by physico-chemical factors affecting the corrosivity of the deep-water masses (depth, temperature, age of the deep water and sediment rate) and by organic coating protecting some particles; IV) the burial depth and diagenesis.

Dissolution processes within the water column and at the sediment-water interface have major effects on microfossil assemblages. Such effects have been intensively investigated using foraminiferal proxies since the 1950s (e.g., Arrhenius,1952; Berger, 1970; Le and Shackleton, 1992). One of the most used dissolution proxy in pelagic sediments is the

planktonic foraminifera fragmentation as defined by Berger (1970). The latter and subsequent studies showed that the fragmentation of planktonic foraminifera increases with depth in the water column under the lysocline, until planktonic foraminiferal remains are completely dissolved beneath the CCD.

The dissolution patterns of calcareous nannofossils have been also studied (e.g., Adelseck et al., 1973; Roth and Berger, 1975; Gibbs et al., 2004, 2010; Beaufort et al., 2007; Jin et al., 2019) but nannofossil-based proxies have been much less frequently used than foraminifera-based proxies to reconstruct deep water corrosivity (Bralower et al., 2014). The relative abundance of calcareous nannofossils is routinely used as a paleoenvironmental proxy, whereas their absolute abundances have been used to reconstruct changes in $CaCO_3$ accumulation through space and time with different methods (e.g., Geisen et al., 1999; Beaufort et al., 2014; Bordiga et al., 2015; Suchéras-Marx et al., 2019a). One of the earliest attempts to use nannofossil fragmentation as dissolution proxy only considered *Discoaster* spp. fragments (Gibbs et al., 2004), which show no significant correlation with other, more classical dissolution proxies. Nannofossil fragments have been also taken into consideration in other studies (Dunkley Jones and Bown, 2007; Gibbs et al., 2010), which again show no clear correlation with dissolution proxies.

A systematic quantification of nannofossil fragmentation has never been attempted likely because it is a time-consuming approach. However, a quantification of the size and abundance of these fragments may help in improving reconstructions of nannofossil absolute abundance and hence their export and burial fluxes. Interestingly, some authors reported that the amount of sedimentary carbonate estimated using the reconstructed masses of entire coccoliths was systematically lower than the total amount of carbonate fine fraction (Bornemann et al., 2003; Ziveri et al., 2007). These authors have already

hypothesised that such discrepancy might be largely attributed to the mass of nannofossils fragments, which are not routinely estimated.

In this work, we present a new method for calculating the fragmentation and incorporate it in total abundance estimates of early Paleogene calcareous nannofossils. Samples come from deep-ocean sediment samples of ODP (Ocean drilling program) Site 1209, covering the upper Thanetian to lower Ypresian (55.6 to 57.4 Ma according to Westerhold et al. 2018). First, we carried out a detailed analysis of the size, nature, number of nannofossil fragments and of entire specimens to quantify their temporal evolution in the studied interval, which comprises several hyperthermal episodes including the PETM. Samples were analysed under a light polarising microscope (LM) and a scanning electron microscope (SEM) in order to compare both methods and detect the influence of possible methodological biases. The fragmentation record was then compared to dissolution proxies based on planktonic foraminifera for the same interval at ODP Site 1209. Finally, we propose a novel method to reconstruct absolute abundances of calcareous nannofossils by including both entire specimens and fragments.

2. Geological setting

Sample studied here come from ODP Site 1209 drilled during Leg 198 on the volcanic submarine high of Shatsky Rise (32° 30.1081'N, 158° 30.3564'E), in the northwestern Pacific Ocean (Bralower et al., 2002) (Fig. 1). Given its position far from land areas and its location in the North Pacific Oceanic gyre, the site received very low detrital input during the Paleogene. Site 1209 was drilled at 2387 m corresponding to a paleodepth of around 1900 m during the PETM (Takeda and Kaiho, 2007). The Paleogene sediments of this site were intensively studied owing to their expanded and continuous sedimentary record (Bralower

et al., 2002). The sediments are mostly unconsolidated and mainly consist of nannofossil ooze in the upper Paleocene (Thanetien) interval and of nannofossil ooze bearing foraminifera during the lower Eocene (Ypresien) interval. Cores were acquired using APC (Advanced Piston Core) method.

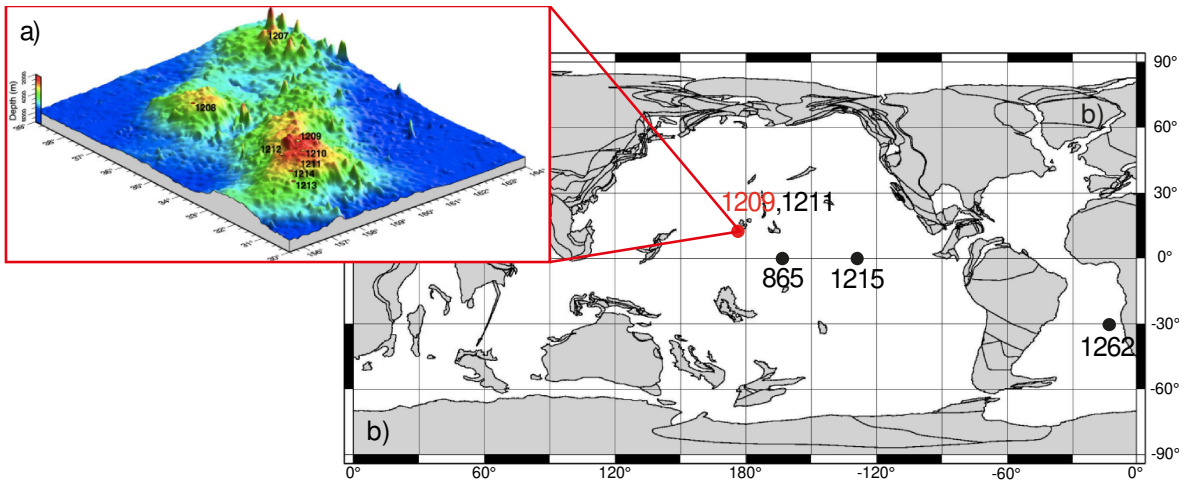

Fig. 1. Location of ODP Site 1209. a) Bathymetry of Leg 198 sites at Shatsky Rise (Bralower et al., 2002); b) Location of ODP Site 1209 (in red) during the PETM and other ODP Sites (in black) cited in the text (56 Ma; www.odsn.de)

3. Material and methods

3.1 Nannofossil samples

Fifty-six samples from holes A, B, and C, dated from the upper Thanetian (Paleocene) to lower Ypresian (Eocene) were studied. Samples from hole A and C (n=46) were selected to cover the entire interval studied, from around 216.8 to 225.0 revised meter composite depth (rmcd) with an average sample resolution of 18 cm. Samples from hole B (n=10), from around 217.7 to 218.1 rmcd covering the PETM onset (218.01 rmcd) were taken with an average sample resolution of 3 cm.

3.2. Slide preparation

Slides were prepared for scanning electron microscopy (SEM) and polarized-light microscope observations (LM) using a slightly modified version of the settling method described by Beaufort et al. (2014). Two cover slides (3.2 x 2.4 cm) and a SEM cover slide (diameter 1.2 cm) were simultaneously placed in the same Petri dish. The two cover slips were weighed before and after settling using a precision microbalance (± 0.00001 g). Dried sediment (5-6 mg) was weighed using the precision microbalance, transferred into a 50 mL Falcon tube and mixed with 40 mL of water. After homogenization, the solution was poured in the Petri dish and let to settle for 4 hours. The water was carefully sucked up with a water-pump and the cover slides were oven-dried at 45°C overnight. Cover slides were glued to microscope slides using Rhodopass B (polyvinyl acetate). The SEM cover slide was fixed to a SEM plot covered by a carbon adhesive. A total of 56 samples were coated with gold-palladium 3nm thick using a Leica EM ACE 200 coater, and were analysed with a Phenom SEM G2 PRO SEM. Among these samples, 28 were analysed with an optical microscope Leica DM 750 P (x1000 magnification).

150 3.3. Nannofossil observation

Particle count was performed on pictures taken directly with the SEM or with a Leica
152 EC3 camera mounted on the optical microscope using the LAS EZ V.3.4.0 software. Nannofossils on SEM and LM pictures were measured with the ImageJ software. Particle
154 counts for SEM and LM were made on a minimum surface of 0.0756 mm^2. This area is considered as representative of the sample, owing to the preliminary rarefaction curve
156 analysis (Appendix A. Raw data). On average, 900 nannofossils and fragments were counted in each sample in LM and SEM. Different categories of nannofossils and fragments
158 (representing half or less than that of the original nannofossil specimen) were considered. The genera *Discoaster, Fasciculithus, Sphenolithus* and their fragments have been
160 differentiated (Appendix B1-B2. Supplementary data). Placoliths, numerically representing the majority of the assemblages, are divided into two size groups (<7µm and ≥7µm; 7µm
162 being around the average size for Paleocene-Eocene assemblages according to Herrmann and Thierstein, 2012). The different genera of placolith were not differentiated. We divided
164 placolith fragments into six different categories (Table 1). The smallest placolith fragments that could be counted are estimated to be around 3% of an entire coccolith, and correspond
166 to a small part of the rim composed of the radial array of crystallites. The different fragment categories allow the reconstruction of a theoretical number of nannofossils represented by
168 fragments. In the following, the reconstructed nannofossil abundance calculated using entire specimens plus the fragments is referred to as “R”. In the analysed sediments, a very small
170 number of reworked Cretaceous specimens are present (less than 0.1% of the assemblage).

	Fragment sizes	Proportion of the originale palcolith	Main placolith genera	SEM pictures
Category 1	<7µm	(3-10%)	*Coccolithus* spp. *Toweius* spp. *Ericsonia* spp. *Umbilicosphaera* spp.	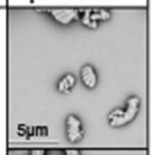
Category 2	<7µm	(11-25%)		
Category 3	<7µm	(26-50%)		
Category 4	≥7µm	(3-10%)	*Coccolithus* spp. *Ericsonia* spp. *Cruciplacolithus* spp. *Chiasmolithus* spp.	
Category 5	≥7µm	(11-25%)		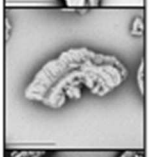
Category 6	≥7µm	(26-50%)		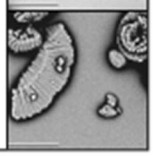

Table. 2. Description of the six different categories of placolith fragments. From the left to the right column are listed: the size of the placolith fragment counted in µm, the percentage that the fragment represents compare to the original placolith in %, the main placolith genera to which the fragments could belong across the late Paleocene at ODP Site 1209, and the SEM pictures of the placolith fragment categories. Scale bar corresponds to 5µm.

3.4. Fragment size distribution

In a given sample, N_1, N_2 and N_3 correspond to the number of fragments counted from respectively 3-10% (categories 1 and 3), 11-25% (categories 2 and 4), 26-50% (categories 3 and 6) of the original placolith whatever the fragment size in µm. From these measurements and assuming that there are no fragments smaller than s_{min} = 0.03 (namely 3%), we can compute the cumulative fraction $P(s)$, defined as the fraction of fragments that are larger than the relative size s:

(1) $P(0.03) = 1$, $P(0.10) = (N_2+N_3)/(N_1+N_2+N_3)$ and $P(0.25) = N_3/(N_1+ N_2+N_3)$

196 Where *N* is the number of fragments of a given size and *P*(*s*) the cumulative fraction of fragment of a given size *s*.

198

We assume that the actual Fragment Size Distribution (FSD) can be described by the 200 continuous function *n*(*s*) giving the number of fragments of size between *s* and *s*+*ds*. If this FSD follows a power law, which is a common pattern in various fragmentation processes 202 (e.g., Åström, 2006), then:

204 (2) $n(s) = k*s^{-m}*ds$

206 Where *m* is the power law index and *k* a normalizing constant, consequently the predicted form for the cumulative fraction is (Appendix B3. Supplementary data):

208

(3) $P(s) = (S_{max}^{1-m} - S^{1-m})/(S_{max}^{1-m} - S_{min}^{1-m})$

210

Where *P*(*s*) is the cumulative fraction of fragment of a given size *s* and *m* the power law 212 index.

214 3.5. Reconstructed abundance of nannofossils based upon entire specimens and fragments

The reconstructed nannofossil abundance (Δ%) is the ratio in percent of the 216 reconstructed nannofossils over the total number of entire nannofossils. It was calculated using the following formula:

218

$$(4)\ \Delta\% = (rn_x/n_x)*100$$

Where Δ% is the reconstructed nannofossil abundance in %, *nx* is the number of specimens of a given taxon and rn_x is the number of specimens reconstructed on the basis of the fragments of the taxon *x*. If the FSD follows a power law of index *m*, we can reconstruct the initial number of specimens before fragmentation (rn_x) by calculating the average size and counting the number of fragments within each size class (Appendix B4. Supplementary data):

$$(5)\ rn_x = ((1-m)/(2-m))*((N_1*((0.10^{2-m}-0.03^{2-m})/(0.10^{1-m}-0.03^{1-m}))+(N_2*((0.25^{2-m}-0.10^{2-m})/(0.25^{1-m}-0.10^{1-m}))+(N_3*((0.50^{2-m}-0.25^{2-m})/(0.50^{1-m}-0.25^{1-m}))))$$

Where rn_x is the number of specimens reconstructed based on the fragments of the taxon *x*, *N* is the number of fragments of a certain size and *m* the power law index.

3.6. Nannofossil fragments and abundance

The proportion of nannofossil fragments (NF%) was calculated according to the planktonic foraminifera fragmentation index of Berger (1970):

$$(6)\ NF\% = (nf/n)*100$$

Where NF% is the proportion of nannofossil fragments in %, *nf* is the number of fragments and *n* is the total number of entire nannofossils and fragments.

Relative abundances of the different nannofossil and fragment groups were calculated using the following formula:

$$(7)\ RA_x = (n_x/n)*100$$

Where RA_x is the relative abundance (%) of a given group, n_x is the number of specimens from the taxon *x*, and *n* is the total number of entire nannofossils or fragments, respectively. The nannofossil absolute abundances, expressed as the number of particles per gram of sediment (n/g), was calculated using a polarized-light microscope (LA_x) and a scanning electron microscope (EA_x).

$$(8)\ LA_x = (n_x*l*h)/(m*A)$$

Where LA_x is the nannofossil absolute abundance (n/g) of a given group based on counts performed under the light microscope (LM); n_x is the number of entire specimens of the taxon x; *l* is the length; *h* is the width of the microscope cover slide in cm; *m* is the sediment mass on the cover slide in grams and *A* is the studied area in the slide (cm^2).

$$(9)\ EA_x = (n_x*\pi*r)/(m*A)$$

Where EA_x is the nannofossil absolute abundance (n/g) of a given group based on counts performed under the SEM and *r* is the radius of the SEM cover slide in cm.

The nannofossil absolute abundances considering entire nannofossils and reconstructed nannofossil (n/g), was calculated using a LM (LAR_x) and a SEM (EAR_x).

$$(10)\ LAR_x = ((n_x+rn_x)*l*h)/(m*A)$$

Where LAR_x is the nannofossil absolute abundance considering entire nannofossils and reconstructed nannofossils using a LM (n/g) of a given group; n_x is the number of entire specimens of the taxon x; rn_x is the number of specimens reconstructed on the basis of the fragments for the taxon *x*; *l* is the length; *h* is the width of the microscope cover slide in cm; *m* is the sediment mass on the cover slide in grams and *A* is the studied area in the slide (cm^2).

$$(11)\ EAR_x = ((n_x+rn_x) * \pi * r)/(m*A)$$

Where EA_x is the nannofossil absolute abundance using a SEM (n/g) and *r* is the radius of the SEM cover slide in cm.

3.7. Coarse fraction, benthic/planktonic ratio and planktonic foraminifera fragmentation

A total of 45 samples (15 of which are the same as the ones used for nannofossil analyses; Appendix A. Raw data) have been analysed for their foraminiferal content. Around 1 g of sediment was soaked in water for 24 hours and sieved at 63 µm. Sample residues were oven-dried at 70°C and weighed using a microbalance (± 0.0001 g) to calculate the amount of coarse fraction (CF%) relative to the bulk sediment. Sediment residues were sieved again at 150 µm and the planktonic foraminifera (entire specimens and fragments) as

290 well as benthic foraminifera were counted under a stereomicroscope. A minimum of 500 planktonic foraminifera were counted for each sample. Planktonic foraminifera
292 fragmentation (PFF%) was calculated using the formula of Berger (1970), i.e. the number of planktonic foraminifera fragments divided by the total number of planktonic foraminifera
294 particles (entire specimens plus fragment). Benthic/planktonic ratios (Benthic%) is the number of benthic foraminifera shell divided by the total number of foraminifera (Arrhenius,
296 1952).

298 3.8. Geochemical analyses

The $\delta^{13}C$ and $\delta^{18}O$ of bulk carbonates (73 samples, comprising 5 replicates; Appendix
300 A. Raw data) were measured using an automatic sampler Multiprep coupled with a dual inlet GV isoprime™ isotope ratio mass spectrometer at the Laboratoire de Géologie de Lyon. On
302 average, a 500 µg aliquot of each sample was weighed with a microbalance (± 0.000001 g) and was reacted with anhydrous phosphoric acid at 90°C for 20 min. Sample measurements
304 were adjusted to the international standard NIST NBS 18 (-5.014 ± 0.076 ‰ $\delta^{13}C_{V\text{-}PDB}$; -23.200 ± 0.146 ‰ $\delta^{18}O_{V\text{-}PDB}$ n=12) and to an in-house Carrara Marble (2.025 ± 0.058 ‰ $\delta^{13}C_{V\text{-}PDB}$; -1.841 ± 0.069 ‰ $\delta^{18}O_{V\text{-}PDB}$ n=21).
306

308 3.9. Statistical errors

Statistical errors in relative abundances are given with 95% confidence intervals as
310 described in Suchéras-Marx et al. (2019b) using the software Past4. Statistical errors (95% confidence intervals and weight error) were propagated to the group absolute abundances.
312 For total absolute abundances, an error bar of 2σ is proposed, where:

314 $$(12)\ \sigma = (1/\sqrt{n})$$

316 With σ the standard error and *n* is the total number of nannofossils.

Using the software Past4, a One Way ANOVA (analysis of variance) was performed to

318 compare the abundance of the nannofossil groups and the fragment groups calculated for common

320 SEM and LM samples

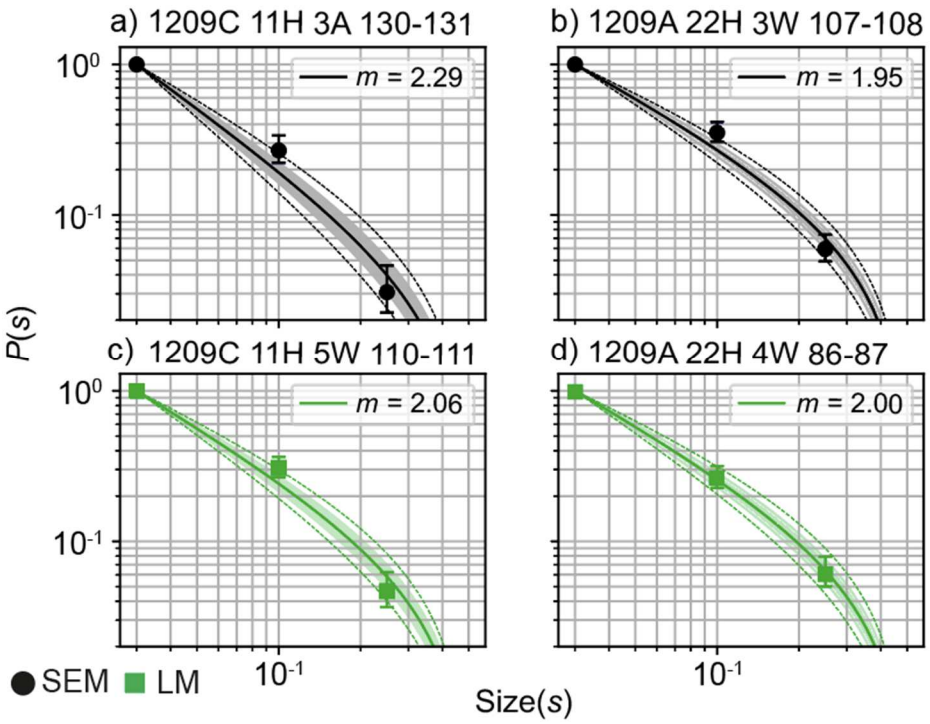

322 (28 in total).

324 **4. Results**

4.1. Fragment

326 size distribution (FSD)

328

330

332

334

Fig. 2. Proportion of fragments with a size larger than *s, P*(*s*), in four samples according to the size (s) of fragment: a) SEM 198-1209C-11H-3A, 130-131; b) SEM 198-1209A-22H-3W, 107-108; c) LM 198-1209C-11H-5W, 110-111; d) LM 198-1209A-22H-4W, 86-87. The straight lines correspond to the best fit given by equation (3), shaded areas to the standard deviation sigma in the value of *m*, while dotted lines correspond to the 2sigma envelop. Error bars correspond to nannofossil count uncertainty.

The variation of *P*(*s*) with fragment size *s* for 4 different samples is illustrated in Figure 2. Data points were adjusted by equation (3) on the figure 2, the power law index *m* being the only free parameter. The FSD of the studied samples can be correctly described by a power law distribution (Fig. 2). The power law index found for the SEM and the LM sample analyses varies from 1.57 to 2.28, with an average value of 1.92 (Fig. 2; Appendix A. Raw data). The average *m* index is higher in LM samples (1.99), than in SEM samples (1.88). This observation unpredictably indicates that the FSD of LM samples is slightly more dominated by small fragments than in the SEM samples.

4.2. Stable isotope measurements

The bulk $\delta^{13}C$ data are consistent with previous measurements of the Paleocene interval at Shatsky Rise (e.g., Cramer et al., 2003; Colosimo et al., 2005; Penman et al., 2014) and extend the record to the upper Paleocene interval. These data notably show repeated shifts toward lower values that correspond to a series of hyperthermal events identified in other deep-sea and hemipelagic successions (e.g., Cramer et al., 2003; Agnini et al., 2016; Luciani et al., 2016; Gutjahr et al., 2017; Westerhold et al., 2018; Barnet et al., 2019). The hyperthermal events are placed according to the $\delta^{13}C_{bulk}$ (Fig. 3a) as defined by Cramer et al.

358 (2003). The D1 and D2 events, previously identified by Westerhold et al. (2018) using benthic foraminifera $\delta^{13}C$ and XRF Fe records, are not seen in the $\delta^{13}C_{bulk}$ record shown here.

360

4.3. Absolute nannofossil abundances

362 Absolute nannofossil abundances calculated with a LM (LA) and with a SEM (EA) follow the same trends, although LA values are systematically lower by about $1x10^9$ n/g than 364 EA values (Fig. 3b, c). The absolute abundance including the reconstructed nannofossils with light and electronic microscopy (LAR and EAR) is, as expected, systematically higher than the 366 absolute abundance of entire nannofossils (from 11 to 63% with an average of 21 and 29% for LM and SEM counts, respectively; Appendix A. Raw data) (Fig. 3b, c). EA and LA are 368 especially low during the PETM with a minimum at around $0.7x10^9$ n/g.

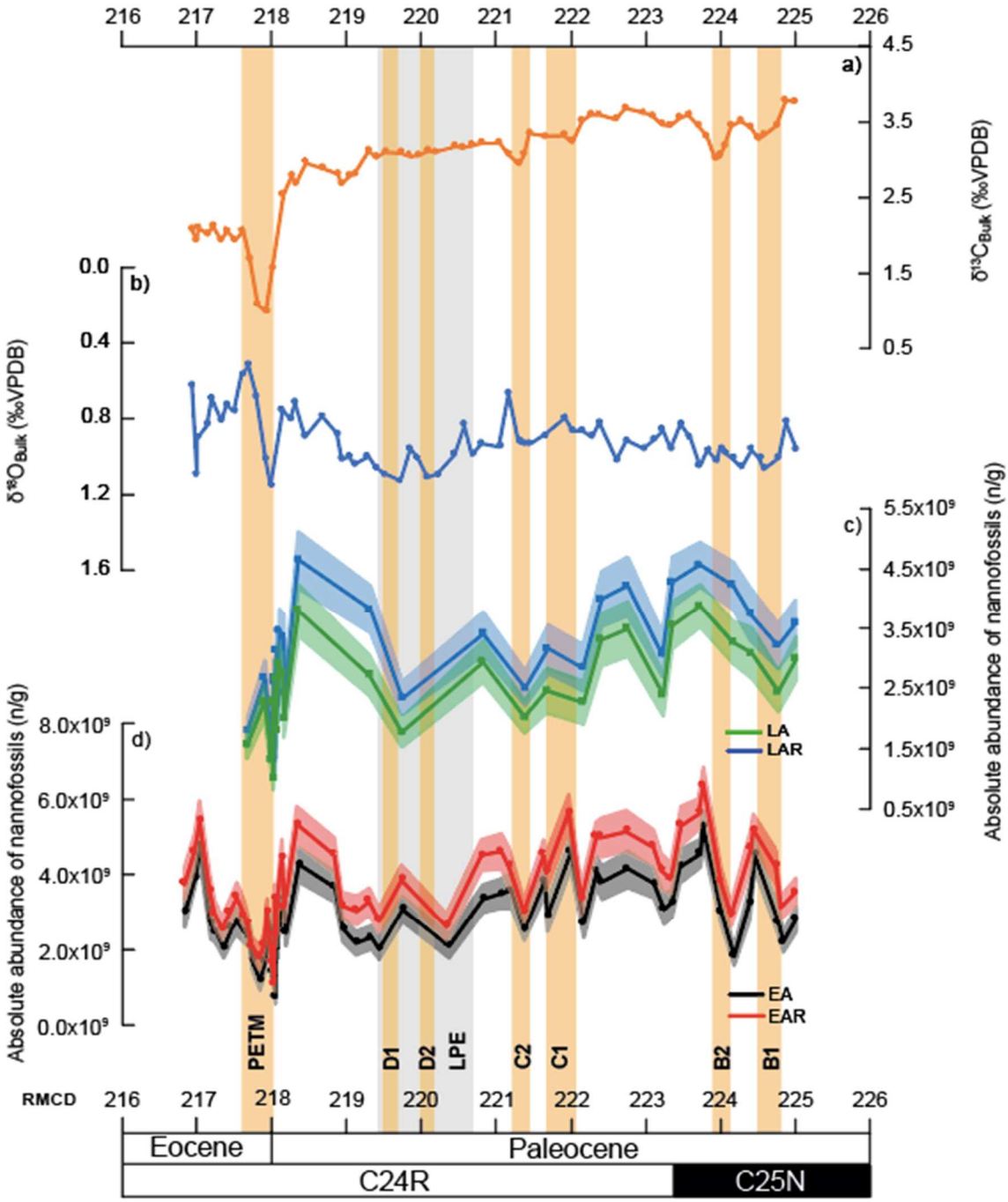

Fig. 3. Geochemical data and nannofossil abundance across the Paleocene-Eocene transition at ODP Site 1209: a) $\delta^{13}C_{Bulk}$ (‰VPDB) record; b) $\delta^{18}O_{Bulk}$ (‰VPDB) record; c) absolute abundances of whole (green) and reconstructed (blue) calcareous nannofossils, as estimated using light microscope; d) absolute abundances of whole (black) and reconstructed (red) calcareous nannofossils as calculated using SEM. Shaded areas correspond to 2sigma as described in section 3.9. Shaded bars in orange indicate the hyperthermal events and shaded bar in grey correspond to the late Paleocene Event (LPE).

370

372

374 4.4. Nannofossil assemblages

4.4.1. Relative and absolute abundances of entire nannofossil groups

376 The absolute abundances of entire specimens issued from SEM and LM counts are similar (Fig. 4a, c, d, e, h, j), except for large placoliths (Fig. 4b, g), which show lower values 378 in LM counts (p <0.01). The SEM counts indicate that small (23-63%) and large (21-51%) placoliths, constitute the bulk of the nannofossils assemblages (Fig. 4f, g). RA of small 380 placoliths broadly show minimum values at the PETM onset (35%) and between 219.4 and 220.7 rmcd (23%), in correspondence of the new event detected in this account and named 382 the "Late Paleocene Event" (LPE) (Fig. 4f).

EA of small placoliths show minimum values through the LPE and the PETM onset 384 (around $0.5x10^9$ n/g and $0.3x10^9$ n/g, respectively) (Fig. 4a).

The RAs of *Discoaster* spp. and *Fasciculithus* spp., calculated in SEM (Fig. 4h, i) follow 386 comparable trends for most of the studied interval. The highest values are recorded across the LPE and at the PETM onset (up to 11 and 20.5% and 10.5 and 17.5% for *Discoaster* spp. 388 and *Fasciculithus* spp. for the LPE and the PETM, respectively). The RA of *Sphenolithus* spp. (Fig. 4j) shows minimum values across the LPE (0.5%). The EAs of *Discoaster* spp., 390 *Fasciculithus* spp. and *Sphenolithus* spp., estimated in SEM broadly show comparable trends compared to their RA (Fig. 4c-e).

392

394

396

398

400

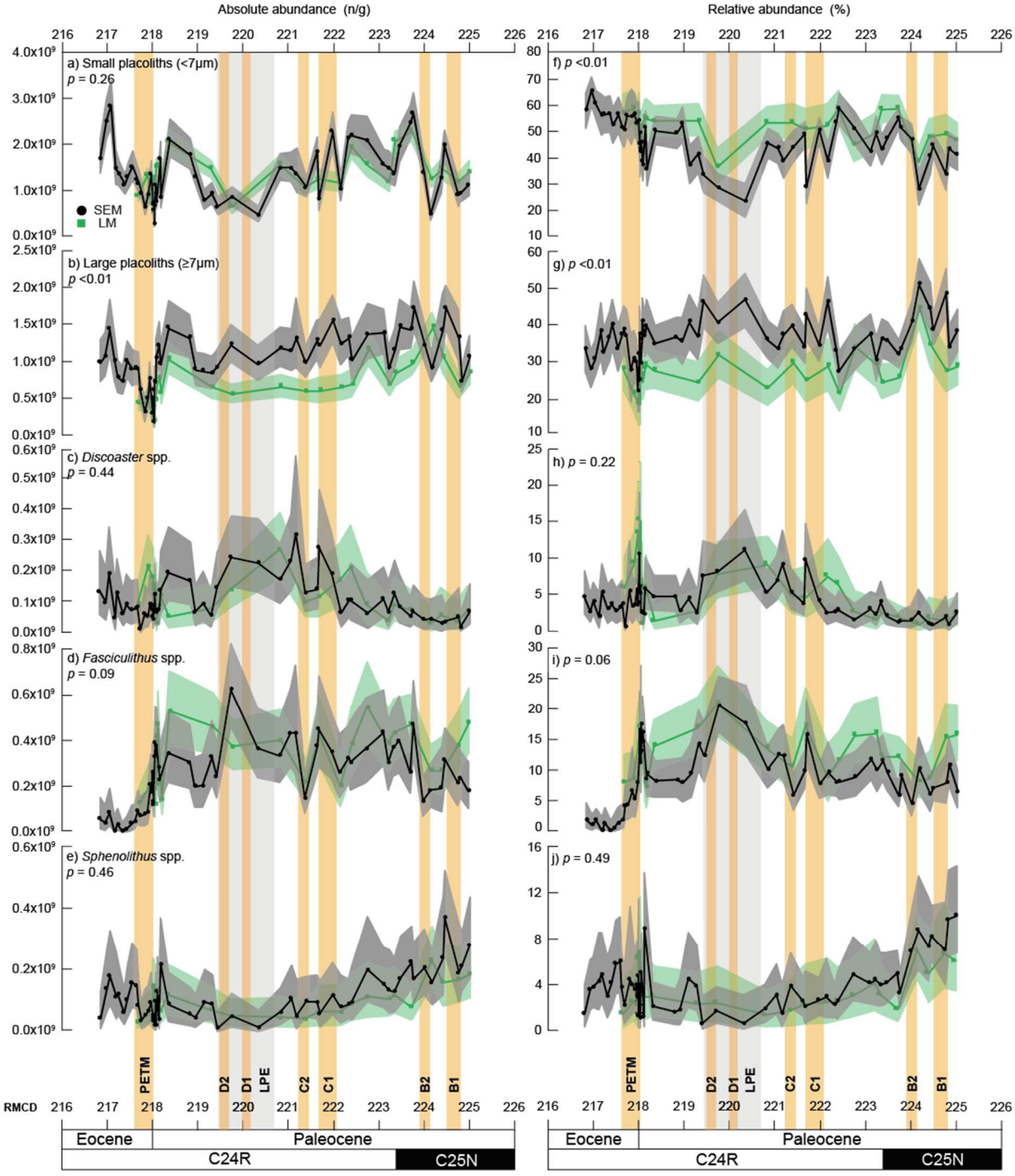

Fig. 4. Absolute (a-e) and relative (f-j) abundances of calcareous nannofossil estimated using SEM (black dots) and light microscope (green squares) counts across the Paleocene-Eocene transition at ODP Site 1209. a, f) small placoliths (<7µm); b, g) large placoliths (≥7µm); c, h) Discoaster spp.*; d, i) Fasciculithus* spp.*; e, j) Sphenolithus* spp.*. Grey and green shaded areas correspond to the 95% confidence intervals (section 3.9). P values are given for each group of nannofossil as described in section 3.9. Shaded bars in orange show the hyperthermal events and the shaded bar in grey indicates the Late Paleocene Event (LPE).*

4.4.2. Relative and absolute abundances of nannofossil fragments

The RAs of different groups of fragments calculated in LM and SEM are similar (Fig. 5h, I, j, l), except for fragments of categories 1 and 6 that show distinct variations (p <0.10) (Fig. 5g, k). Fragments of categories 1 and 2 dominate the assemblage of nannofossil fragments (50-77% and 14-39% respectively) (Fig. 5g, h).

Fragments of category 1 show in SEM minimum and maximum values (50 and 77%) across the LPE and at the base of PETM interval, respectively. EA of fragments of categories 1-3 (Fig. 5a-c) shows in general similar variations between each-other with very low values across the PETM and, to a lesser extent, within the LPE.

The RAs of fragments of categories 5-6 and *Discoaster* spp. fragments follow relatively similar trends (Fig. 5d-f), with the highest values recorded across the LPE and at the PETM onset. EAs of fragments of category 5 and *Discoaster* spp. fragments present similar trends (Fig. 5d, f).

414

416

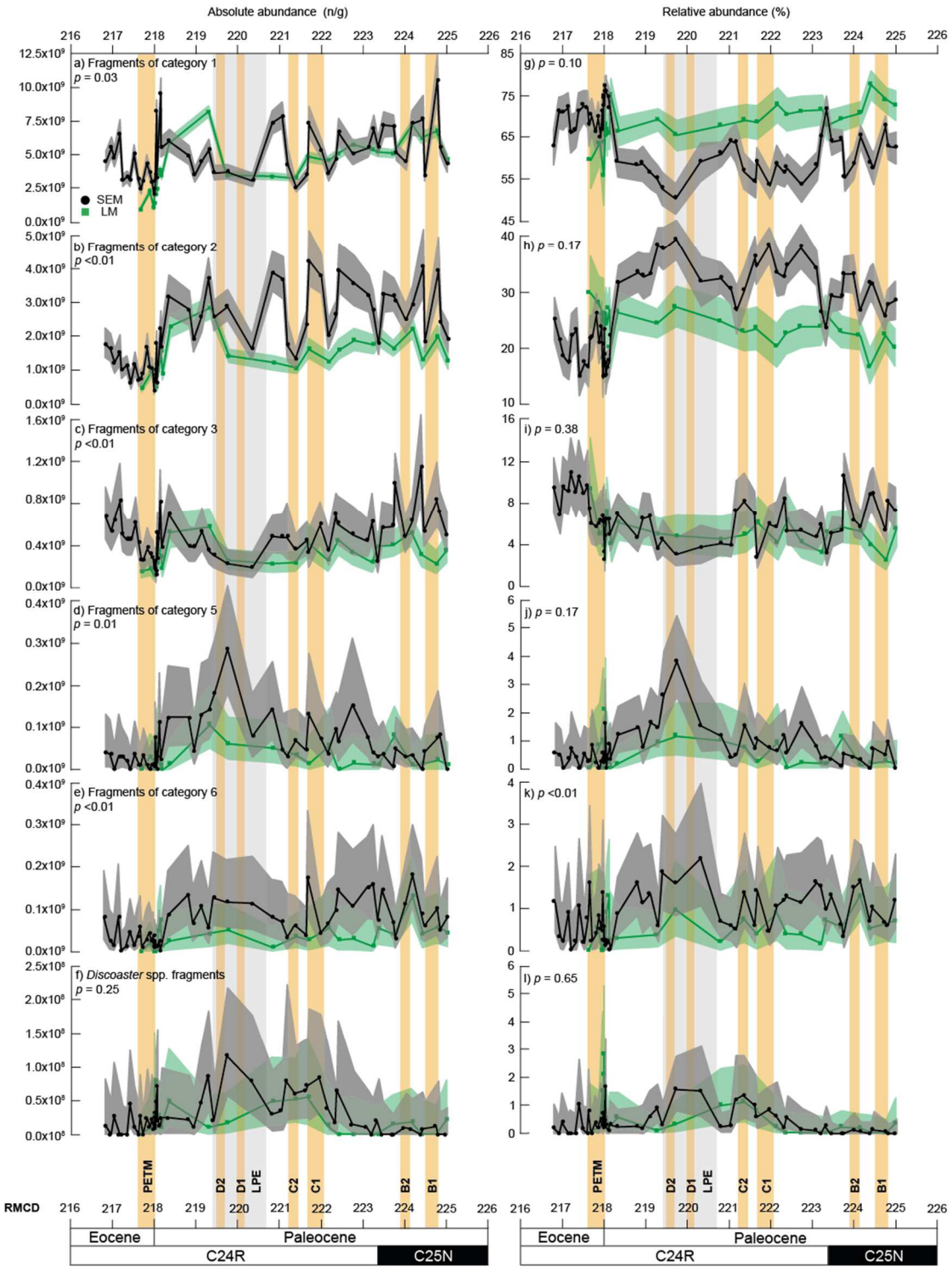

Fig. 5. Absolute (a-f) and relative (g-i) abundances of calcareous nannofossil fragments estimated using SEM (black dots) and under optical microscope (green squares) across the Paleocene-Eocene transition at ODP Site 1209. a, g) fragments of category 1; b, h) fragments of category 2; c, i) fragments of category 3; d, j) fragments of category 5; e, k) fragments of category 6; f, l) Fragments of Discoaster spp.*. Grey and green shaded areas correspond to the 95% confidence intervals (section 3.9). P values are given for each group of fragments as described in section 3.9. Shaded bars in orange show the hyperthermal events and the shaded bar in grey indicates the Late Paleocene Event (LPE)*

418 4.6. Dissolution proxies and nannofossil fragmentation

The sediment coarse fraction (CF%) we calculated follows the same trend previously
420 published by Westerhold et al. (2018) (Fig. 6f) and generally shows opposite trends with respect to planktonic foraminifera fragmentation (Fig. 6e). PFF%, and Benthic% show high
422 values from around 219.4 to 220.7 rmcd corresponding to the LPE (Fig. 6d-f).

The NF% values are slightly higher in SEM counts than in LM counts. SEM-based NF% values
424 show an average value of 70% of the total particle content (e.g., fragments plus entire nannofossil specimens). A marked increase to 85% is recorded slightly before the PETM
426 onset (Fig. 6a). Nannofossil fragments do not co variate well with CF%, PFF% and benthic% (Fig. 6d-f). Fragmentation of small and large placoliths seem to better co-variate with
428 foraminifera-based dissolution proxies than NF% across the LPE (Fig. 6b, c).

430

432

434

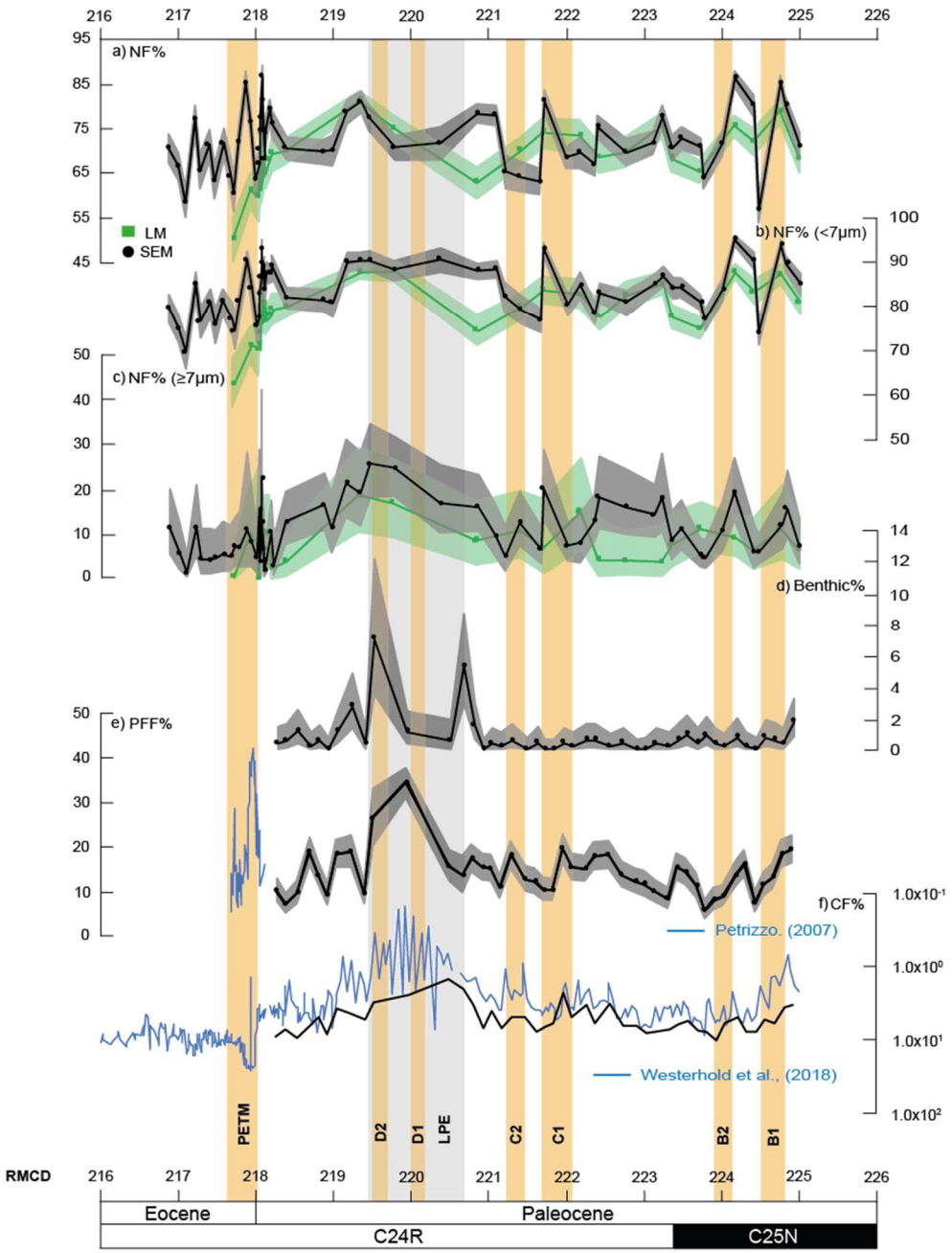

Fig. 6. Comparison between nannofossil fragmentation and dissolution proxies across the Paleocene-Eocene transition at ODP Site 1209: a) nannofossil fragmentation (NF%) as calculated using SEM (black dots) and LM (green squares); b) small placolith fragmentation (NF% <7µm); c) large placolith fragmentation (NF% ≥7µm); d) Benthic foraminifera index (Benthic%); e) Planktonic foraminifera fragmentation (PFF%) and *Morozovella* spp. fragmentation (blue) from Petrizzo (2007); f) Coarse fraction (CF%) from this study (black) and from Westerhold et al. (2018)(blue). Grey and green shaded areas correspond to the 95% confidence intervals (section 3.9). Error bars for coarse fraction related to weighing, being very small, are given in Appendix A. Raw data. Shaded bars in orange indicate the hyperthermal events and shaded bar in grey corresponds to the Late Paleocene Event (LPE).

460 **5. Discussion**

5.1. A new approach to reconstruct nannofossil abundance

462 The SEM and LM counts of placolith fragments in the Thanetian-Ypresian interval provide us a useful method to reconstruct an all-inclusive absolute abundance of 464 nannofossils (entire nannofossils and reconstructed nannofossils using fragments). Ziveri et al. (2007) and Bornemann et al. (2003) noticed that the nannofossil $CaCO_3$ wt.% estimates 466 based upon the masses and absolute abundances of entire nannofossils were systematically lower (1.5 to 4 times lower) than the bulk-rock $CaCO_3$ wt.% measured in sediments. These 468 authors suggested that this systematic underestimation of nannofossil contribution to the carbonate fine fraction is largely due to the occurrence of fragments, which are not routinely 470 counted.

Our results demonstrate an underestimation of the nannofossils absolute abundance 472 by 29% and 21% on average according to estimations made under SEM and LM, respectively (minimum and maximum values: 11% to 63%; Fig. 7), when only entire nannofossils are 474 considered. The Δ% between the abundance calculated using LM and SEM shows an excellent correlation with nannofossils fragmentation (Fig. 7). Our data shows an excellent 476 agreement with the theoretical relation between Δ% and NF% predicted from the FSD power-law model (Fig. 7; see Appendix B3-4 for details):

478

$$(12)\ \Delta\% = (NF\%/(\eta(100-NF\%))*100)$$

480

With η a dimensionless parameter (as defined by equation (10) of the Appendix B3. 482 Supplementary data).

A key implication of this finding is that absolute abundances can be calculated using the equation in Fig. 7, without requiring a detailed counting of distinct fragment classes, provided future work confirms that the fragmentation process of placoliths universally follows the power law FSD of index m~2 found for Paleogene strata at Site 1209. As fragmentation of placoliths appears to follow a breakup law commonly found in various physical processes (e.g., Bitelli et., 1999; Aström et al., 2004), changes in nannofossil assemblages should theoretically influence the proportion of fragments in the assemblage

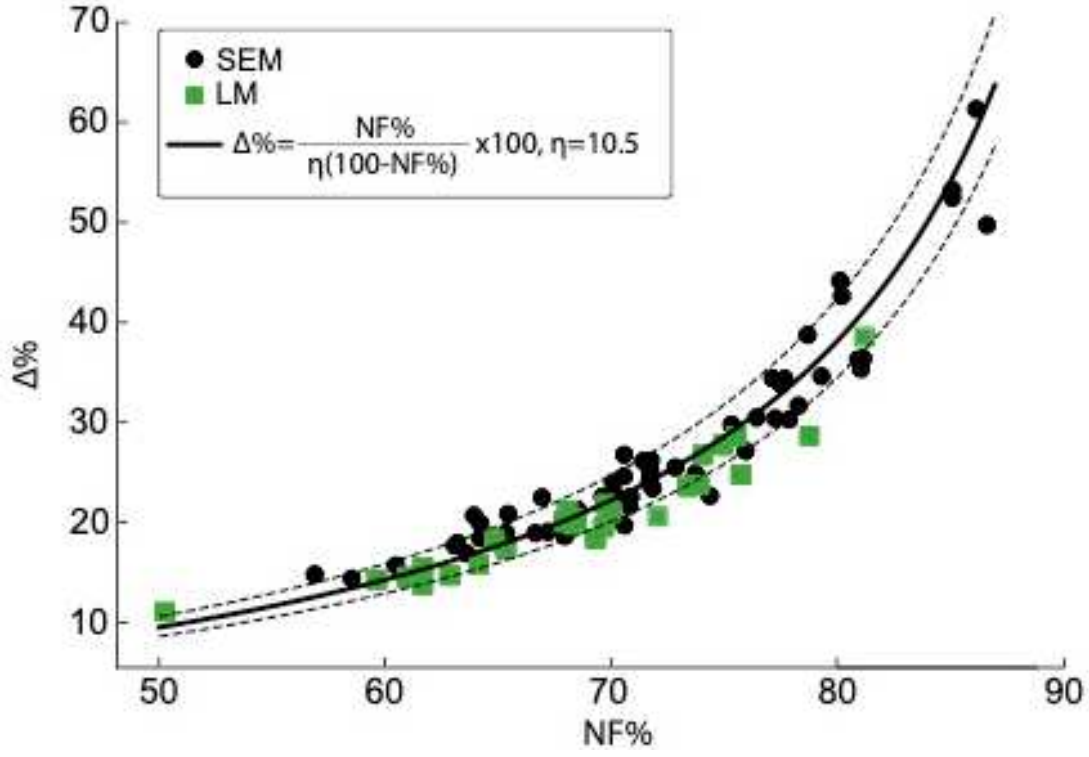

Fig. 7. Relationships between Δ% (the reconstructed nannofossil abundance in %) and the nannofossils fragmentation (NF%) for SEM and LM observations. Equation 5 (see section 3.5) is used to calculated the number of reconstructed nannofossil and thus Δ% (equation 4). Since 99% of the nannofossil fragments are placolith fragments (Appendix A. Raw data), we assume here that the nannofossil fragments follow the same break-up law as the placolith fragments. The black line corresponds to the theoretical prediction of equation (12) with m = 1.92 (see section 4.1). The best fit by the same expression with η as a free parameter leads to $\eta = 10.8$, very close to the theoretical prediction. For sake of clarity, this curve is not plotted here. Average 95% confidence intervals are given in the Appendix A. Raw data. Black dotted lines correspond to equation with $m \pm \sigma_m$

(NF%) but not the relationship between the nannofossils fragmentation and the reconstructed nannofossil abundance in % (Δ%).

494

5.2. Stratigraphic changes in fragment distribution and nannofossil assemblages across the
496 Thanetien-Ypresien interval

5.2.1. Dissolution proxies, nannofossil fragments and assemblages across hyperthermal
498 events

The studied interval records several greenhouse gas-driven hyperthermal events
500 during which the CCD and lysocline likely shoaled globally (e.g., Kirtland Turner et al., 2014; Westerhold et al., 2018). There is a general agreement that the carbonate coarse fraction in
502 deep-sea sediments decreases with increasing dissolution due to the preferential breakup and dissolution of planktonic foraminifera (Bassinot et al., 1994). At Site 1209, stratigraphic
504 changes in the coarse fraction (this study; Westerhold et al., 2018) correlates well with foraminiferal-based dissolution proxies (this study; Hancock and Dickens, 2005; Petrizzo,
506 2007). As Petrizzo (2007) used a 125 µm sieve for the fragmentation of *Morozovella*, only a relative comparison of PFF% is relevant.

508 There is no systematic increase in the nannofossil fragmentation, coarse fraction and the planktonic foraminifera fragmentation observed during the hyperthermal events B1, B2, C1
510 and C2, described by Cramer et al. (2003). D1 and D2 events being included in the Late Paleocene Event, they are not considered here.

512 All dissolution proxies (CF%, PFF% and Benthic%) display similar temporal changes, and point to a maximum in dissolution over a 1.3 m-thick interval (from 219.4 rmcd to
514 around 220.7 rmcd) in the upper Paleocene. This interval of high dissolution, pre-dating the PETM (55.93 Ma) by about 300 to 700 kyrs (corresponding to around 56.27 to 56.66 Ma
516 according to the age model of Westerhold et al., 2008; 2018), was previously identified

based on a lower-resolution record (Hancock and Dickens, 2005; Westerhold et al., 2011), but never examined in detail.

The NF% values are relatively stable or, even, they slightly decrease across the LPE interval where all foraminiferal fragmentation proxies point to maximum dissolution (Fig. 6). The decrease in NF% values is due to the increase of large taxa (*Discoaster* spp. and *Fasciculithus* spp.) (Fig. 4.c, d). However, NF% of small and large placoliths NF% are both high across the LPE (Fig. 6b, c).

An increase in nannofossil fragmentation could reflect higher dissolution due to bottom water corrosivity (Beaufort et al., 2007), higher zooplankton grazing in the water column (Honjo 1976; Knappertsbusch and Brummer, 1995; Broerse et al., 2000), or increased lithostatic pressure during burial (Feazel et al., 1985, Hirano et al., 2001). The intensity of zooplankton grazing is yet poorly quantifiable for fossil samples and the lithostatic diagenesis intensity can be assumed as relatively constant over the short (<9m) studied part of the Paleocene (Appendix B5. Supplementary data). The high placolith fragmentation recorded during the LPE could be related to dissolution in agreement with dissolution proxies (Fig. 6b, c). Such an explanation is consistent with the increased of *Discoaster* spp. percentages across the LPE, along with the decrease in relative abundance of small placoliths. Indeed, as dissolution is selective, an early dissolution may drive a partial or total disaggregation of the elements composing a given nannofossil (Adelsek et al., 1973; Hill, 1975; Honjo 1975, 1976; Roth and Berger, 1975; Thierstein, 1980). *Discoaster* spp. was reported to be more resistant to dissolution than other nannofossils (Adelseck et al., 1973; Gibbs et al., 2004; Raffi and De Bernardi, 2008). These latter studies have even suggested that *Discoaster* spp. specimens tend to become overgrown (receptors) along with increasing dissolution of solution-susceptible coccoliths (donors). Thierstein (1980) reported similar

dissolution susceptibility for small nannoliths of Late Cretaceous-Early Paleogene age. Thus, the ratio small placoliths/*Discoaster* spp. could represent a valuable dissolution proxy, as suggested by D'Onofrio et al. (2016) who used the *Toweius* spp./*Discoaster* spp. ratio to track dissolution events in lower Eocene sediment from Italy. The relative increase in percentage of *Fasciculithus* spp. across the LPE interval appears similar to that seen in *Discoaster* spp. and could also be partially due to its resistance to dissolution. Nevertheless, a very similar increase in *Fasciculithus* spp. was reported in several contemporaneous sites recording very different dissolution conditions (Site 1262), suggesting that this increase at least partially reflects evolutionary or ecological trends. In this regard, the ratios between nannofossil taxa, classically used to establish indices of past ecological parameters, should be ideally used with independent dissolution proxies (e.g., this study, Gibbs et al., 2004).

Another interesting aspect of the studied interval at Site 1209 is the sharp rise of the planktonic foraminifera fragmentation pattern reported by Petrizzo (2007) across the PETM onset, which indicates an intense episode of dissolution. Conversely, the same interval records a marked increase in CF% (blue curve in Fig. 6f; Westerhold et al., 2018), suggesting a sharp decrease in dissolution. The latter is at odds with the increase in dissolution across the PETM, which was interpreted based on several pieces of evidence in many oceanic sites (e.g., Zachos et al., 2005; Luciani et al., 2007; Petrizzo, 2007; Alegret et al., 2009; Gibbs et al., 2010; Kelly et al., 2010). This anomalous abundance of CF% at Site 1209 at the onset of PETM interval could therefore reflect a peculiar sedimentary pattern, such as the preferential winnowing of the fine-grained nannofossil-ooze fraction resulting from a transient increase in bottom current intensity (Bralower et al., 2014). A similar mechanism was also suggested to explain the rise in CF% recorded at ODP Site 865 (Arreguin-Rodriguez et al., 2016). The CF% peak at Site 1209 could also be explained by a higher planktonic

foraminifera flux (Battacharya et al., 2021). As an alternative explanation, we suggest that this increase in CF% could reflect a transient episode of low nannoplankton productivity or export.

A strong increase in NF% is only observed in SEM across the PETM onset, which could result from an intense dissolution. LM data show a peak of NF% during the PETM but the sampling resolution is lower than for the SEM analysis. The PETM onset is associated with the increase in RA of *Discoaster* spp., which parallels the decrease in percentage of small placoliths. *Discoaster* spp. overgrowth intensity is also higher during the PETM than across the rest of the studied interval (Appendix B5. Supplementary data). All together these observations point to an episode of strong dissolution in the water column or within the sediment across the PETM onset, suggesting that the CCD shoaling might have been more important than commonly interpreted for ODP Site 1209 (Colosimo et al., 2005; Zeebe and Zachos, 2007; Westerhold et al. 2018).

5.2.2. The Late Paleocene Event, causes and extent

The nannofossil assemblages studied in this work show a marked increase in the RAs of *Discoaster* spp. and *Fasciculithus* spp. and a decrease in RA of small placoliths in the interval between 219.4 m and 220.7 m, corresponding to the LPE (Thanetian; Fig. 4f, h, i). A very similar increase was reported in the work of Alvarez et al. (2019) for Discoasterales during the LPE at the same site. Raffi et al. (2005) also recorded an increase in the abundance of *Discoaster* spp. at ODP Site 1215 (North Pacific). This interval at Site 1209 records a maximum in foraminiferal fragmentation, Benthic%, and very low CF% values (this study; Hancock and Dickens, 2005; Westerhold et al., 2018). The LPE shows therefore

588 changes similar to the PETM for the majority of the considered parameters, with the exception of CF% (see section 5.2.1.).

590 Hancock and Dickens (2005), based on a lower resolution PFF%, CF% and Benthic% proxies from ODP Site 1209 and from the nearby ODP Site 1211, reported a similar period of 592 dissolution over the LPE. Conversely, the coarse fraction record at Site ODP 1262 (South Atlantic; Littler et al., 2014) does not show any marked decrease during the interval 594 correlative to the LPE. The LPE might then be a relatively local event restricted to the North Pacific. The stable isotope record of benthic foraminifera *Nuttallides truempyi* and of the 596 bulk sediment generated at site 1209 (this study; Westerhold et al., 2018) shows no abrupt change in $\delta^{13}C$ values during this interval, nor significant decrease in $\delta^{18}O$ which would 598 indicate a warming event. Given the extremely low amount of organic matter content at site 1209 (Bralower et al., 2002), dissolution related to CO_2 released by organic matter 600 degradation is unlikely. Benthic foraminiferal assemblages as an index of deep-water oxygenation were analysed at DSDP site 577 (Shatsky Rise) but the low resolution does not 602 allow to draw any conclusions (Kaiho, 1991). At ODP Site 865 (equatorial Pacific), dysoxic or anoxic condition were not recorded based upon benthic foraminifera assemblages during 604 the LPE (Arreguin-Rodriguez et al., 2016).

Because of its limited geographic extent, ocean acidification related to massive carbon 606 release during the LPE seems unlikely to be the main cause for carbonate dissolution. Alternatively, the LPE could have been caused by a shift from young to old deep-water 608 masses, the latter being richer in CO_2 and hence more corrosive against carbonates. However, such an enrichment in CO_2 due to the influx of older bottom-water masses should 610 have led to a ^{13}C depletion recorded by benthic foraminifera calcite. This depletion is not evident when looking at the benthic isotope data compiled by Westerhold et al. (2018).

612 Additionally, the low-resolution neodymium isotope records of the Pacific Ocean (Thomas, 2004; Thomas et al., 2008; 2014) indicate rather stable deep-water circulation in the late 614 Paleocene. Nevertheless, we cannot discard the possibility that the LPE resulted from two initially distinct events (D1 and D2), which were homogenised by bioturbation into a 616 stratigraphically broader event. This would imply that D1 and D2 were much more intense in the Pacific than in other sites (e.g., Walvis Ridge). This is key to determining location and 618 duration of intense dissolution events, as it could give us insights into the cause of hyperthermal like the PETM. The drop in nannofossil and fragment absolute abundances 620 (Figs. 4-6) show a larger magnitude at the PETM than that recorded across the LPE, but the latter occurs over a much wider stratigraphic interval. It seems, therefore, that these two 622 events of increased dissolution were driven by different mechanisms and biogeochemical feedbacks.

624

6. Conclusions

626 The detailed analysis of nannofossil fragments in the studied Paleocene-Eocene samples indicates that nannofossil absolute abundances of entire specimens underestimate by ~25% 628 the actual number of nannofossils contained in the sediment, i.e., those represented by all nannofossil particles, including small fragments. This finding has strong implications for 630 reconstructions of past nannofossil export and burial fluxes. The reconstructed abundances of whole specimens show an excellent relationship with nannofossil fragmentation in 632 stratigraphic data, implying that nannofossil break-up follows a general physical law. Thus, all-inclusive nannofossil abundances per gram of sediment can be easily calculated by 634 applying this relationship on raw fragment and whole nannofossil counts, i.e., without a detailed counting of different-sized fragment. Although very promising, this relationship was

however established on samples from a single locality, covering a relatively short time interval. The methodology proposed herein should therefore be applied to different nannofossil assemblages from different localities and ages, containing distinct coccolith and nannolith morphologies, before it can be safely extrapolated to other assemblages.

The percentage of nannofossil fragments across the Paleocene-Eocene transition at ODP Site 1209 does not show a clear relationship with the well-established foraminiferal dissolution proxies (PFF%, CF%, Benthic%), confirming that nannofossil fragmentation represents a poor tracer of dissolution. By contrast, the fragmentation of large placoliths and the small placoliths/*Discoaster* spp. ratio seem to be more reliable markers for dissolution, which complement the well-established foraminiferal dissolution proxies. Together, the foraminiferal and nannofossil assemblage data at ODP Site 1209 indicate a marked rise in dissolution across the PETM onset and during a longer-lived episode referred to in this study as the LPE (Lower Paleocene Event), which predates the PETM onset by about 300-700 kyrs and includes the hyperthermal D1 and D2. This hitherto poorly documented event differs from the PETM in that it seems more restricted geographically, it is not associated with evidence for global warming nor massive carbon injection, and was clearly longer-lived.

Acknowledgments

The authors are thankful to the IODP (International Ocean Discovery Program) for providing the ODP 1209 samples. We thank Maria Rose Petrizzo for sharing the planktonic foraminifera fragmentation (data shown in Fig. 6e), Frederic Quillévéré for the help in supervising Alissa Mehir's internship and Bruno Andre for the careful proofread of the manuscript. Eddy Buiron research has been possible thanks to a Laboratoire de Géologie de Lyon scholarship. This research was funded by the Institut Universitaire de France, the ANR

660 OXYMORE (ANR-18-CE31-0020), and the INSU Tellus 2022. This manuscript is a part of Nicolas Pige PhD project, funded by the French Ministry of Research

662

Author Contributions

Nicolas Pige: Conceptualization, Methodology, Formal analysis (overgrown quantification, isotope, nannofossil reconstruction), Investigation, Data Curation, Writing - Original Draft, Review **Guillaume Suan:** Conceptualization, Investigation, Writing, Review, Funding acquisition **Eddy Buiron:** Conceptualization, Methodology, Formal analysis (stratigraphic nannofossil counts), Investigation **Vincent Langlois:** Methodology, Formal analysis (nannofossil reconstruction), Writing, Review **Alyssa Mehir:** Formal analysis (foraminiferal-based dissolution proxies) **Arnauld Vinçon-Laugier:** Formal analysis (isotope), Review **Emanuela Mattioli:** Conceptualization, Investigation, Writing, Review, Funding acquisition

Declaration of Competing interest

None

References

Adelseck, C.G., Geehan, G.W., Roth, P.H., 1973. Experimental Evidence for the Selective Dissolution and Overgrowth of Calcareous Nannofossils During Diagenesis. *GSA Bulletin* 84, 2755–2762. https://doi.org/10.1130/0016-7606(1973)84<2755:EEFTSD>2.0.CO;2.

Agnini, C., Spofforth, D. J. A., Dickens, G. R., Rio, D., Pälike, H., Backman, J., Muttoni, G., Dallanave, E., 2016. Stable isotope and calcareous nannofossil assemblage record of the late Paleocene and early Eocene (Cicogna section). *Climate of the Past* 12, 883–909. doi:10.5194/cp-12-883-2016.

Alegret , L., Ortiz , S., Orue-Etxebarria , X., Bernaola, G., Baceta, J.I., Monechi, S., Apellaniz, E., Pujalte, V., 2009. The Paleocene-Eocene Thermal Maximum: new data on microfossil turnover at the Zumaia section, Spain. *Palaios* 24, 318-328. https://doi.org/10.2110/palo.2008.p08-057r.

Alvarez, S.A., Gibbs, S.J., Bown, P.R., Kim, H., Sheward, R.M., Ridgwell, A., 2019. Diversity decoupled from ecosystem function and resilience during mass extinction recovery. *Nature* 574, 242–245. https://doi.org/10.1038/s41586-019-1590-8.

Andruleit, H., 1996. A Filtration Technique for Quantitative Studies of Coccoliths. *Micropaleontology* 42, 403–406. https://doi.org/10.2307/1485964.

Archer, D.E., Maier-Reimer, E., 1994. Effect of deep-sea sedimentary calcite preservation on atmospheric CO2 concentration. *Nature* 367, 260e263.

Arreguín-Rodríguez, G.J., Alegret, L.., Thomas, E., 2016. Late Paleocene-middle Eocene benthic foraminifera on a Pacific seamount (Allison Guyot, ODP Site 865): Greenhouse climate and superimposed hyperthermal events. *Paleoceanography* 31, 346–364. https://doi.org/10.1002/2015PA002837.

Arrhenius, G. 1952. Sediment cores from the East Pacific. *Reports of the Swedish Deep-Sea Expedition*, 1947–1948, 5, 1–228.

Åström, J.A., Linna, R.P., Timonen, J., Møller, P.F., Oddershede, L., 2004. Exponential and power-law mass distributions in brittle fragmentation. *Physical Review*. E 70, 026104. https://doi.org/10.1103/PhysRevE.70.026104.

Åström, J.A., 2006. Statistical models of brittle fragmentation. *Advances in Physics* 55, 247–278. https://doi.org/10.1080/00018730600731907.

Balch, W., Drapeau, D., Bowler, B., Booth, E., 2007. Prediction of pelagic calcification rates using satellite measurements. *Deep Sea Research Part II: Topical Studies in Oceanography* 54, 478–495. https://doi.org/10.1016/j.dsr2.2006.12.006.

Barnet, J., Littler, K., Westerhold, T., Kroon, D., Leng, M., Bailey, I., Röhl, U., Zachos, J.C., 2019. A High-Fidelity Benthic Stable Isotope Record of Late Cretaceous–Early Eocene Climate Change and Carbon-Cycling. *Paleoceanography and Paleoclimatology* 34, 672–691. https://doi.org/10.1029/2019PA003556.

Bassinot, F.C., Beaufort, L., Vincent, E., Labeyrie, L.D., Rostek, F., Müller, P.J., Quidelleur, X., Lancelot, Y., 1994. Coarse fraction fluctuations in pelagic carbonate sediments from the tropical Indian Ocean: A 1500-kyr record of carbonate dissolution. *Paleoceanography* 9, 579–600. https://doi.org/10.1029/94PA00860.

Baumann, K.-H., Bockel, B., Frenz, M., 2004. Coccolith contribution to South Atlantic carbonate sedimentation. In: *Coccolithophores*. Springer, Berlin, pp. 367–402.

Beaufort, L., Probert, I., Buchet, N., 2007. Effects of acidification and primary production on coccolith weight: Implications for carbonate transfer from the surface to the deep ocean. *Geochemistry, Geophysics, Geosystems* 8. https://doi.org/10.1029/2006GC001493.

Beaufort, L., Barbarin, N., Gally, Y., 2014. Optical measurements to determine the thickness of calcite crystals and the mass of thin carbonate particles such as coccoliths. *Nature protocols* 9, 633–42. https://doi.org/10.1038/nprot.2014.028.

Berger, W.H., 1970. Planktonic Foraminifera: Selective solution and the lysocline. *Marine Geology* 8, 111–138. https://doi.org/10.1016/0025-3227(70)90001-0.

Bhattacharya, J., Yeung, L.Y., Cong, L., Dickens, G.R., Sun, T., 2021. Size-Fraction-Specific Stable Isotope Variations as a Framework for Interpreting Early Eocene Bulk Sediment Carbon Isotope Records. *Paleoceanography and Paleoclimatology* 36, e2020PA004132. https://doi.org/10.1029/2020PA004132.

Bordiga, M., Bartol, M., Henderiks, J., 2015. Absolute nannofossil abundance estimates: Quantifying the pros and cons of different techniques. *Revue de Micropaléontologie* 58, 155–165. https://doi.org/10.1016/j.revmic.2015.05.002.

Bornemann, A., Aschwer, U., Mutterlose, J., 2003. The impact of calcareous nannofossils on the pelagic carbonate accumulation across the Jurassic–Cretaceous boundary. *Palaeogeography, Palaeoclimatology*, Palaeoecology 199, 187–228. https://doi.org/10.1016/S0031-0182(03)00507-8.

Bralower, T.J., Premoli Silva, I., Malone, M.J., et al., 2002. *Proceedings of the Ocean Drilling Program, Initial Reports,* 198: College Station, TX (Ocean Drilling Program). doi:10.2973/odp.proc.ir.198.2002.

Bralower, T.J., Kelly, D.C., Gibbs, S., Farley, K., Eccles, L., Lindemann, T.L., Smith, G.J., 2014. Impact of dissolution on the sedimentary record of the Paleocene–Eocene thermal maximum. *Earth and Planetary Science Letters* 401, 70–82. https://doi.org/10.1016/j.epsl.2014.05.055.

Broerse, A.T.C., Ziveri, P., Honjo, S., 2000. Coccolithophore (–CaCO 3) flux in the Sea of Okhotsk: seasonality, settling and alteration processes. Marine Micropaleontology 39, 179–200. https://doi.org/10.1016/S0377-8398(00)00020-7.

Cartapanis, O., Galbraith, E.D., Bianchi, D., Jaccard, S.L., 2018. Carbon burial in deep-sea sediment and implications for oceanic inventories of carbon and alkalinity over the last glacial cycle. *Climate of the Past* 14, 1819–1850. https://doi.org/10.5194/cp-14-1819-2018.

Colosimo, A.B., Bralower, T., Zachos, J.C., 2005. Evidence for lysocline shoaling at the Paleocene/Eocene Thermal Maximum on Shatsky Rise, Northwest Pacific. T.J. Bralower, I. Premoli Silva, M.J. Malone (Eds.), *Proceedings of the Ocean Drilling Program, Scientific Results* 198, Ocean Drilling Program, Texas (2006), pp. 1-36.

Cramer, B.S., Wright, J.D., Kent, D.V., Aubry, M.-P., 2003. Orbital climate forcing of δ13C excursions in the late Paleocene–early Eocene (chrons C24n–C25n). *Paleoceanography* 18. https://doi.org/10.1029/2003PA000909.

Dedert, M., Stoll, H., Kars, S., Young, J.R., Shimizu, N., Kroon, D., Lourens, L., Ziveri, P., 2014. Temporally variable diagenetic overgrowth on deep-sea nannofossil carbonates across Palaeogene hyperthermals and implications for isotopic analyses. *Marine Micropaleontology* 107, 18–31. https://doi.org/10.1016/j.marmicro.2013.12.004.

D'Onofrio, R., Luciani, V., Fornaciari, E., Giusberti, L., Boscolo Galazzo, F., Dallanave, E., Westerhold, T., Sprovieri, M., Telch, S., 2016. Environmental perturbations at the early Eocene ETM2, H2, and I1 events as inferred by Tethyan calcareous plankton (Terche section, northeastern Italy). *Paleoceanography* 31, 1225–1247. https://doi.org/10.1002/2016PA002940.

Dunkley Jones, T., Bown, P.R., 2007. Post-sampling dissolution and the consistency of nannofossil diversity measures: A case study from freshly cored sediments of coastal Tanzania. *Marine Micropaleontology* 62, 254–268. https://doi.org/10.1016/j.marmicro.2006.09.001.

Feazel, C.T., Keany, J., Peterson, R.M., 1985. Cretaceous and Tertiary Chalk of the Ekofisk Field Area, Central North Sea, in: Roehl, P.O., Choquette, P.W. (Eds.), *Carbonate Petroleum Reservoirs*, Casebooks in Earth Sciences. Springer, New York, NY, pp. 495–507. https://doi.org/10.1007/978-1-4612-5040-1_32.

Geisen, M., Bollmann, J., Herrle, J.O., Mutterlose, J., Young, J.R., 1999. Calibration of the random settling technique for calculation of absolute abundances of calcareous nannoplankton. *Micropaleontology* 45, 437–442.

Gibbs, S.J., Shackleton, N.J., Young, J.R., 2004. Identification of dissolution patterns in nannofossil assemblages: A high-resolution comparison of synchronous records from Ceara Rise, ODP Leg 154. *Paleoceanography* 19, PA1029. https://doi.org/10.1029/2003PA000958.

Gibbs, S.J., Stoll, H.M., Bown, P.R., Bralower, T.J., 2010. Ocean acidification and surface water carbonate production across the Paleocene–Eocene thermal maximum. *Earth and Planetary Science Letters* 295, 583–592. https://doi.org/10.1016/j.epsl.2010.04.044.

Gutjahr, M., Ridgwell, A., Sexton, P.F., Anagnostou, E., Pearson, P.N., Pälike, H., Norris, R.D., Thomas, E., Foster, G.L., 2017. Very large release of mostly volcanic carbon during the Palaeocene–Eocene Thermal Maximum. *Nature* 548, 573–577. https://doi.org/10.1038/nature23646.

Hancock, H., Dickens, G., 2005. Carbonate dissolution episodes in Paleocene and Eocene sediment, Shatsky Rise, West-Central Pacific. T.J. Bralower, I. Premoli Silva, M.J. Malone (Eds.), *Proceedings of the Ocean Drilling Program: Scientific Results* 198, Texas A & M University, College Station (2005), pp. 1-24.

Hay, W.W., 2004. Carbonate fluxes and calcareous nannoplankton. Thierstein, H., Young, J. (Eds.), *Coccolithophores: From Molecular Processes to Global Impact*. Springer, Berlin (2004), pp. 509–528.

Herrmann, S., Thierstein, H.R., 2012. Cenozoic coccolith size changes—Evolutionary and/or ecological controls? *Palaeogeography, Palaeoclimatology, Palaeoecology* 333–334, 92–106. https://doi.org/10.1016/j.palaeo.2012.03.011.

Hill, M.E., 1975. Selective Dissolution of Mid-Cretaceous (Cenomanian) Calcareous Nannofossils. *Micropaleontology* 21, 227–235. https://doi.org/10.2307/1485025.

Hirano, S., Ogawa, Y., Kawamura, K., 2001. Deformation of unlithified sediments in an early stage of the compaction process deduced from microtextures and magnetic fabrics: ODP Leg 174B, Hole 1074A. Becker, K., Malone, M.J. (Eds.), *Proceedings of the Ocean Drilling Program. Scientific Results*, 174B (2001), 1–13.

Honjo, S., 1975. Dissolution of suspended coccoliths in the deep-sea water column and sedimentation of coccolith ooze. in: *Cushman Foundation For Foraminiferal Research*, Special Publication 13, 114-128.

Honjo, S., 1976. Coccoliths: Production, transportation and sedimentation. *Marine Micropaleontology* 1, 65–79. https://doi.org/10.1016/0377-8398(76)90005-0.

Honjo, S., Erez, J., 1978. Dissolution rates of calcium carbonate in the deep ocean; an in-situ experiment in the North Atlantic Ocean. *Earth and Planetary Science Letters* 40, 287–300. https://doi.org/10.1016/0012-821X(78)90099-7.

Jin, X., Liu, C., Zhang, H., 2019. Coccolith morphological and assemblage responses to dissolution in the recent sediments of the East China Sea. *Marine Micropaleontology* 152, 101709. https://doi.org/10.1016/j.marmicro.2018.09.001.

Kaiho, K., 1991. Global changes of Paleogene aerobic/anaerobic benthic foraminifera and deep-sea circulation. *Palaeogeography, Palaeoclimatology, Palaeoecology* 83, 65–85. https://doi.org/10.1016/0031-0182(91)90076-4.

.

Kelly, D.C., Nielsen, T.M.J., McCarren, H.K., Zachos, J.C., Röhl, U., 2010. Spatiotemporal patterns of carbonate sedimentation in the South Atlantic: Implications for carbon cycling during the Paleocene–Eocene thermal maximum. Palaeogeography, Palaeoclimatology, Palaeoecology 293, 30–40. https://doi.org/10.1016/j.palaeo.2010.04.027.

Kennett, J.P., Stott, L.D., 1991. Abrupt deep-sea warming, palaeoceanographic changes and benthic extinctions at the end of the Palaeocene. *Nature* 353, 225–229. https://doi.org/10.1038/353225a0.

Kirtland Turner, S., Sexton, P.F., Charles, C.D., Norris, R.D., 2014. Persistence of carbon release events through the peak of early Eocene global warmth. *Nature Geosciences* 7, 748–751. https://doi.org/10.1038/ngeo2240.

Knappertsbusch, M., Brummer, G.J.A., 1995. A sediment trap investigation of sinking coccolithophorids in the North Atlantic. *Deep Sea Research Part I*: *Oceanographic Research Papers* 42, 1083–1109. https://doi.org/10.1016/0967-0637(95)00036-6.

Langer, G., Nehrke, G., Jansen, S., 2007. Dissolution of *Calcidiscus leptoporus* coccoliths in copepod guts? A morphological study. *Marine Ecology Progress Series* 331, 139–146. https://doi.org/10.3354/meps331139.

Le, J., Shackleton, N.J., 1992. Carbonate Dissolution Fluctuations in the Western Equatorial Pacific During the Late Quaternary. *Paleoceanography* 7, 21–42. https://doi.org/10.1029/91PA02854.

Littler, K., Röhl, U., Westerhold, T., Zachos, J.C., 2014. A high-resolution benthic stable-isotope record for the South Atlantic: Implications for orbital-scale changes in Late Paleocene–Early Eocene climate and carbon cycling. *Earth and Planetary Science Letters* 401, 18–30. https://doi.org/10.1016/j.epsl.2014.05.054.

Luciani, V., Giusberti, L., Agnini, C., Backman, J., Fornaciari, E., Rio, D., 2007. The Paleocene–Eocene Thermal Maximum as recorded by Tethyan planktonic foraminifera in the Forada section (northern Italy). Marine Micropaleontology 64, 189–214. https://doi.org/10.1016/j.marmicro.2007.05.001.

Luciani, V., Dickens, G.R., Backman, J., Fornaciari, E., Giusberti, L., Agnini, C., D'Onofrio, R., 2016. Major perturbations in the global carbon cycle and photosymbiont-bearing planktic foraminifera during the early Eocene. *Climate of the Past* 12, 981–1007. https://doi.org/10.5194/cp-12-981-2016.

Luo, Y., Boudreau, B.P., Dickens, G.R., Sluijs, A., Middelburg, J.J., 2016. An alternative model for CaCO3 over-shooting during the PETM: Biological carbonate compensation. *Earth and Planetary Science Letters* 453, 223–233. https://doi.org/10.1016/j.epsl.2016.08.012.

Milliman, J.D., Troy, P.J., Balch, W.M., Adams, A.K., Li, Y.H., Mackenzie, F.T., 1999. Biologically mediated dissolution of calcium carbonate above the chemical lysocline? *Deep Sea Research Part I: Oceanographic Research Papers* 46, 1653–1669. https://doi.org/10.1016/S0967-0637(99)00034-5.

Penman, D.E., Hönisch, B., Zeebe, R.E., Thomas, E., Zachos, J.C., 2014. Rapid and sustained surface ocean acidification during the Paleocene-Eocene Thermal Maximum. *Paleoceanography* 29, 357–369. https://doi.org/10.1002/2014PA002621.

Petrizzo, M.R., 2007. The onset of the Paleocene–Eocene Thermal Maximum (PETM) at Sites 1209 and 1210 (Shatsky Rise, Pacific Ocean) as recorded by planktonic foraminifera. *Marine Micropaleontology* 63, 187–200. https://doi.org/10.1016/j.marmicro.2006.11.007.

Raffi, I., Backman, J., Pälike, H., 2005. Changes in calcareous nannofossil assemblages across the Paleocene/Eocene transition from the paleo-equatorial Pacific Ocean. *Palaeogeography, Palaeoclimatology, Palaeoecology* 226, 93–126. https://doi.org/10.1016/j.palaeo.2005.05.006.

Raffi, I., De Bernardi, B., 2008. Response of calcareous nannofossils to the Paleocene–Eocene Thermal Maximum: Observations on composition, preservation and calcification in sediments from ODP Site 1263 (Walvis Ridge — SW Atlantic). *Marine Micropaleontology* 69, 119–138. https://doi.org/10.1016/j.marmicro.2008.07.002.

Roth P.H., Thierstein H.R., 1972. Calcareous nannoplankton: Leg 14 of the Deep Sea Drilling Project. Hayes D.E., Pimm A.C., *et al.* (Eds.), *Initial Reports of the Deep Sea Drilling Project* 14, U.S. Government Printing Office, Washington, D.C (1972). pp. 421-485.

Roth, P., Berger, W., 1975. Distribution and dissolution of coccoliths in the south and central pacific., in: *Cushman Foundation For Foraminiferal Research*, Special Publication 13, 87-113.

Saavedra-Pellitero, M., Flores, J.A., Baumann, K.H., Boeckel, B., Sierro, F.J., 2011. Comparison of different preparation and analysis techniques for quantitative coccolith studies focusing on biogeographic patterns of species. *Micropaleontology* 57, 139–161.

Schlanger, S. O., Douglas, R. G., 1975. The pelagic ooze-chalk-limestone transition and its implications for marine stratigraphy. *Pelagic Sediments: on Land and under the Sea*, 117-148.

Suchéras-Marx, B., Mattioli, E., Allemand, P., Giraud, F., Pittet, B., Plancq, J., Escarguel, G., 2019a. The colonization of the oceans by calcifying pelagic algae. *Biogeosciences* 16, 2501–2510, https://doi.org/10.5194/bg-16-2501-2019.

Suchéras-Marx, B., Escarguel, G., Ferreira, J., Hammer, Ø., 2019b. Statistical confidence intervals for relative abundances and abundance-based ratios: Simple practical solutions for an old overlooked question. *Marine Micropaleontology* 151, 101751. https://doi.org/10.1016/j.marmicro.2019.101751.

Sulpis, O., Jeansson, E., Dinauer, A., Lauvset, S.K., Middelburg, J.J., 2021. Calcium carbonate dissolution patterns in the ocean. *Nature Geoscience* 14, 423–428. https://doi.org/10.1038/s41561-021-00743-y.

Takeda, K., Kaiho, K., 2007. Faunal turnovers in central Pacific benthic foraminifera during the Paleocene–Eocene thermal maximum. *Palaeogeography, Palaeoclimatology, Palaeoecology* 251, 175–197. https://doi.org/10.1016/j.palaeo.2007.02.026.

Thierstein, H.R., 1980. Selective dissolution of late cretaceous and earliest tertiary calcareous nannofossils: Experimental evidence. *Cretaceous Research* 1, 165–176. https://doi.org/10.1016/0195-6671(80)90023-3.

Thomas, D.J., 2004. Evidence for deep-water production in the North Pacific Ocean during the early Cenozoic warm interval. *Nature* 430, 65–68. https://doi.org/10.1038/nature02639.

Thomas, D.J., Lyle, M., Moore Jr., T.C., Rea, D.K., 2008. Paleogene deepwater mass composition of the tropical Pacific and implications for thermohaline circulation in a greenhouse world. *Geochemistry*, *Geophysics*, *Geosystems* 9, Q02002. https://doi.org/10.1029/2007GC001748.

Thomas, D.J., Korty, R., Huber, M., Schubert, J.A., Haines, B., 2014. Nd isotopic structure of the Pacific Ocean 70–30 Ma and numerical evidence for vigorous ocean circulation and ocean heat transport in a greenhouse world. *Paleoceanography* 29, 454–469. https://doi.org/10.1002/2013PA002535.

Westerhold, T., Röhl, U., Raffi, I., Fornaciari, E., Monechi, S., Reale, V., Bowles, J., Evans, H.F., 2008. Astronomical calibration of the Paleocene time. *Palaeogeography, Palaeoclimatology, Palaeoecology* 257, 377–403. https://doi.org/10.1016/j.palaeo.2007.09.016.

Westerhold, T., Röhl, U., Donner, B., McCarren, H.K., Zachos, J.C., 2011. A complete high-resolution Paleocene benthic stable isotope record for the central Pacific (ODP Site 1209). *Paleoceanography* 26, PA2216. https://doi.org/10.1029/2010PA002092.

Westerhold, T., Röhl, U., Donner, B., Zachos, J.C., 2018. Global Extent of Early Eocene Hyperthermal Events: A New Pacific Benthic Foraminiferal Isotope Record From Shatsky Rise (ODP Site 1209). *Paleoceanography and Paleoclimatology* 33, 626–642. https://doi.org/10.1029/2017PA003306.

Young, J. R., Ziveri, P., 2000. Calculation of coccolith volume and it use in calibration of carbonate flux estimates. *Deep sea research Part II: Topical studies in oceanography* 47, 9-11, 1679-1700.

Zachos, J.C., Röhl, U., Schellenberg, S.A., Sluijs, A., Hodell, D.A., Kelly, D.C., Thomas, E., Nicolo, M., Raffi, I., Lourens, L.J., McCarren, H., Kroon, D., 2005. Rapid Acidification of the Ocean During the Paleocene-Eocene Thermal Maximum. *Science* 308, 1611–1615. https://doi.org/10.1126/science.1109004.

Zeebe, R.E., Zachos, J.C., 2007. Reversed deep-sea carbonate ion basin gradient during Paleocene-Eocene thermal maximum. *Paleoceanography* 22, PA3201. https://doi.org/10.1029/2006PA001395.

Zeebe, R.E., 2012. History of Seawater Carbonate Chemistry, Atmospheric CO2, and Ocean Acidification. Annual Review of *Earth and Planetary Sciences* 40, 141–165. https://doi.org/10.1146/annurev-earth-042711-105521.

Ziveri, P., De Bernardi, B., Baumann, K.H., Stoll, H.M., Mortyn, P.G., 2007. Sinking of coccolith carbonate and potential contribution to organic carbon ballasting in the deep ocean. *Deep Sea Research Part II: Topical Studies in Oceanography* 54, 659–675. https://doi.org/10.1016/j.dsr2.2007.01.006.